Check for updates

Advanced Materials

ADVANCED MATERIALS
www.advmat.de

RESEARCH ARTICLE

Polyphosphates-Based Cathode-Electrolyte Interphase for 4.65 V $LiCoO_2$

Hengyu Ren[1] | Xiaohu Wang[1] | Wenwei Cai[1] | Wenguang Zhao[1] | Kunchen Xie[1] | Dongwen Zou[1] | Tao Zeng[1] | Funing Yu[2] | Zhikang Deng[3] | Haocong Yi[1] | Chunyu Xu[1] | Wenhua Zhang[4] | Shunning Li[1,5] | Qinghe Zhao[1,2] | Feng Pan[1]

[1]School of Advanced Materials, Peking University Shenzhen Graduate School, Peking University, Shenzhen, China | [2]College of Physics and Energy, Fujian Normal University, Fuzhou, China | [3]Department of Chemistry, The University of Hong Kong, Hong Kong, China | [4]National Synchrotron Radiation Laboratory, University of Science and Technology of China, Hefei, China | [5]Department of Chemical and Biological Engineering, The Hong Kong University of Science and Technology, Hong Kong, China

Correspondence: Hengyu Ren (renhengyu@pku.edu.cn) | Qinghe Zhao (katong880109@163.com) | Feng Pan (panfeng@pkusz.edu.cn)

Received: 29 January 2026 | **Revised:** 2 April 2026 | **Accepted:** 7 April 2026

Keywords: CEI | covalent interaction | high-voltage $LiCoO_2$ | polyphosphates | targeted construction

ABSTRACT

The stable interfacial chemistry of $LiCoO_2$ (LCO) is the cornerstone for its high-voltage operation. However, interfacial side reactions, originating from the Co/O catalytic sites, lead to ethylene carbonate (EC) oxidation, lithium hexafluorophosphate ($LiPF_6$) hydrolysis, and LCO surface degradation. Herein, we propose that the formation of functional phosphate derivatives (FPD) in the electrolyte, which are generated from the reaction between tris(trimethylsilyl) phosphate (TMSP) and PF_6^- anions, can achieve targeted regulation of the polyphosphates cathode-electrolyte interphase (CEI). During cycling, the FPD spontaneously forms covalent interactions with surface Co/O sites, triggering in situ polymerization that constructs a robust and full-coverage CEI on LCO. The resulting CEI is enriched with polyphosphates and LiF/Li_2O, which ensures high thermodynamic stability and fast Li^+ transport kinetics simultaneously. Consequently, the LCO with optimized electrolyte (1.0 M $LiPF_6$ in fluoroethylene carbonate (FEC)-based solvents with 2.0 wt.% TMSP) demonstrates exceptional cell performance with a high capacity retention of 81.0% after 3000 cycles within 3.0–4.6 V (vs. Li/Li^+), 81.6% after 2000 cycles within 3.0–4.65 V, and shows the feasibility in the LCO||graphite pouch cell with a retention of 80.0% after 500 cycles. This work provides a new insight into the uniform CEI construction for high-voltage LCO cathodes through functional electrolyte engineering.

1 | Introduction

Lithium cobalt oxide ($LiCoO_2$, LCO), as a pioneering and dominant cathode material, has been the cornerstone of commercial lithium-ion batteries for decades [1]. By elevating the charge cutoff voltage (≥4.6 V, vs. Li/Li^+), LCO delivers a significantly enhanced specific capacity and energy density, which is paramount for meeting the ever-growing demands of next-generation high-energy-density applications, such as portable electronic devices, high-performance power tools, and unmanned aerial vehicles [2]. However, high-voltage LCO suffers from severe interfacial side reactions in conventional lithium hexafluorophosphate ($LiPF_6$)/ethylene carbonate (EC)-based electrolytes, a problem similar to that encountered with high-nickel cathodes. Its highly delithiated surface, with catalytic transition metal and oxygen ions, sets off a harmful chain of reactions

Hengyu Ren and Xiaohu Wang. contributed equally to this work.

© 2026 Wiley-VCH GmbH

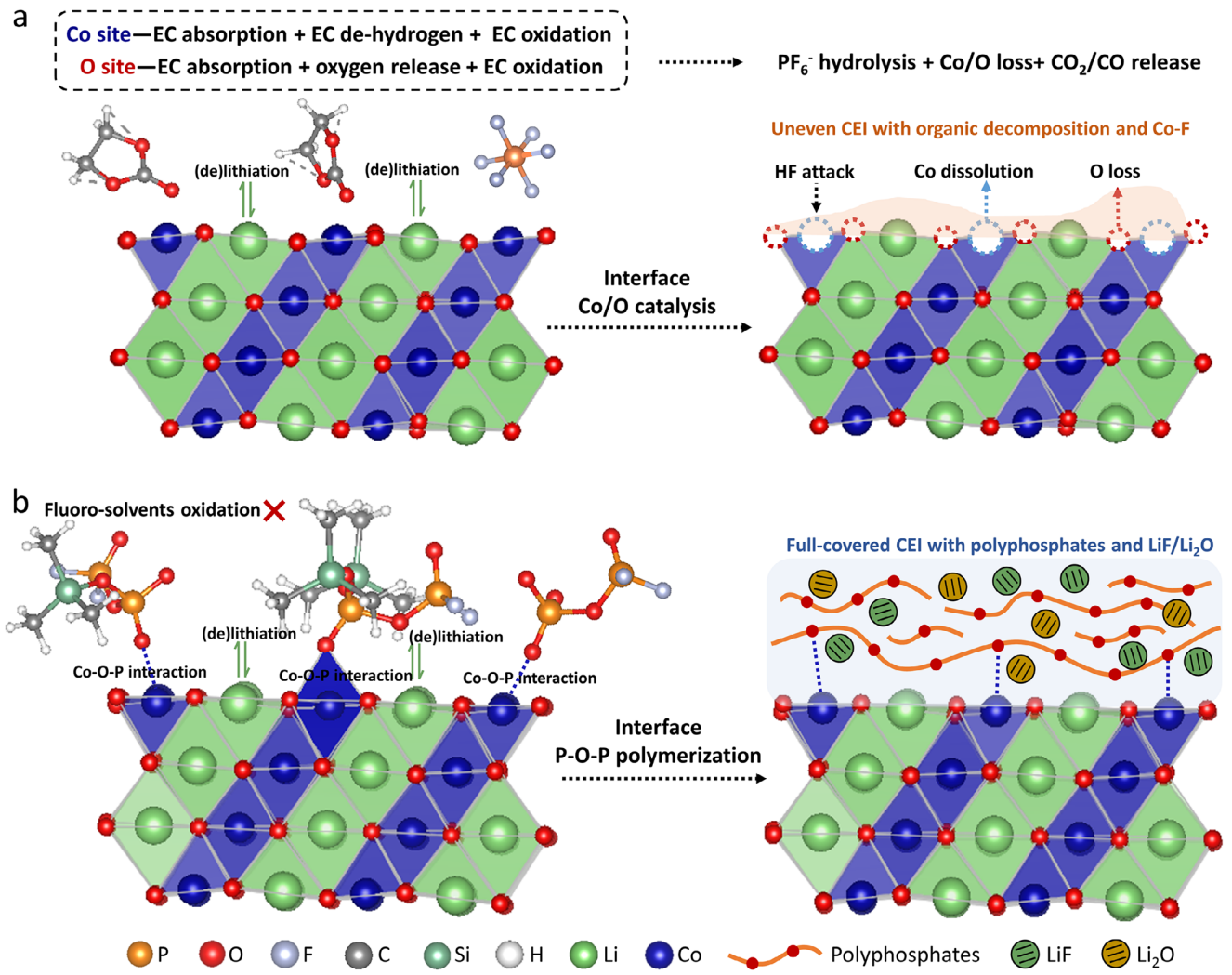

FIGURE 1 | (a) Irreversible lattice oxygen loss and cobalt dissolution from LCO due to catalytic/oxidative effects of surface Co/O sites at the cathode-electrolyte interface. (b) Targeted stabilization through FPD-induced Co—O—P covalent bonding and in situ construction of a full-coverage polyphosphate/LiF/Li_2O integrated CEI.

[3–5]. Specifically, EC molecules adsorb onto the surface via O_{EC}-$Co_{lattice}$ or C_{EC}-$O_{lattice}$ interactions, leading to dehydrogenation or chemical oxidation by released oxygen. The former leads to corrosive HF, whereas the latter produces CO_2, CO, and H_2O, and the resulting water subsequently hydrolyzes $LiPF_6$ to form additional HF [6–9]. This process leads to irreversible lattice oxygen loss and cobalt dissolution of LCO (Figure 1a; Figure S1) [10, 11]. Therefore, stabilizing high-voltage LCO requires atomic-scale inhibition of the catalytic/oxidative effects of Co and O at high voltages. This is essential for maintaining surface structural integrity and ensuring reversible Li^+ (de)intercalation, thereby improving the reversibility of the high-voltage phase transitions (O3–H1-3–O1) [12, 13].

The in situ electrochemical reconstruction of the cathode-electrolyte interphase (CEI) during cycling presents an ideal strategy for applying a uniform coating on high-voltage LCO, leveraging the electrolyte's innate ability to permeate the cathode [14]. Recent research has demonstrated that lithium salts, additives, or solvents featuring specific functional groups can decompose to form CEI films enriched with components such as LiF, LiN_xO_y, Li_3PO_4, or polymers, etc [15–19]. These films exhibit promising protective qualities and favorable Li^+ transport kinetics [20, 21]. However, the potential-driven decomposition of electrolyte components is often unable to be precisely controlled, frequently resulting in a CEI layer with inconsistent chemical composition and uneven thickness [20–22]. To address this issue, a more targeted approach involves directing the interfacial reaction by harnessing molecular-level interactions between electrolyte functional groups and the Co/O sites on the LCO surface [23]. For instance, Fan et al. constructed a specific Co—CN interfacial coupling using cyano groups, while a recent study established a Co—O—Si bond through the in situ decomposition of a cyclic siloxane [24, 25]. Both strategies effectively stabilize the surface lattice of LCO, thereby suppressing the dissolution of transition metal ions and the loss of lattice oxygen. Thus, the development of low-cost, "targeted" surface modification strategies that can further guide the formation of an optimized CEI composition represents a vital pathway toward structurally stable, practical LCO cathodes operating at ultra-high voltages.

15214095, 0, Downloaded from https://advanced.onlinelibrary.wiley.com/doi/10.1002/adma.73065 by University Town Of Shenzhen, Wiley Online Library on [19/04/2026]. See the Terms and Conditions (https://onlinelibrary.wiley.com/terms-and-conditions) on Wiley Online Library for rules of use; OA articles are governed by the applicable Creative Commons License

In this work, we introduce the functional phosphate derivatives (FPD) in the electrolyte, including fluorophosphate and oligophosphate, etc., to achieve targeted regulation of the CEI for high-voltage LCO (Figure 1b). The FPD additives are generated prior to cycling via a substitution reaction between tris(trimethylsilyl) phosphate (TMSP) and PF_6^- anions. These species subsequently induce the formation of a covalent Co—O—P interaction at the LCO surface during electrochemical operation. Furthermore, the surface-bound FPD undergoes in situ polymerization, resulting in a composite CEI architecture enriched with polyphosphates, LiF, and Li_2O. This unique structure combines robust mechanical strength, high thermodynamic stability, and efficient Li^+ transport kinetics. When coupled with the oxidation-resistant solvent fluoroethylene carbonate (FEC), this tailored electrolyte system enables exceptional cycling stability for high-voltage LCO. This system delivers ultra-stable electrochemical performance, achieving a high capacity retention of 81.0% after 3000 cycles within 3.0–4.6 V, 81.6% after 2000 cycles within 3.0–4.65 V in LCO||Li cells, and demonstrates practical feasibility in an LCO||graphite pouch cell, which retains 80.0% of its capacity after 500 cycles.

2 | Formation Mechanism of FPD

FEC exhibits better oxidation stability compared to EC, which effectively suppresses the oxidative decomposition of cyclic carbonates at high-voltage LCO-electrolyte interfaces while concurrently contributing to anode interface stability, as previously reported [4]. To significantly enhance the cycling stability of high-voltage LCO, we replaced EC with FEC as the cyclic carbonate solvent and introduced TMSP as an additive to induce the formation of FPD species. Conventional linear carbonates, ethyl methyl carbonate (EMC) and diethyl carbonate (DEC), were selected as co-solvents to optimize the ionic conductivity and viscosity of the electrolyte. Thus, the electrolyte formulations designed for this study comprise three systems for a controlled comparison (Figure 2a): the BE electrolyte (1.0 M $LiPF_6$ in EC/EMC/DEC, 3:4:3 by volume), the FE electrolyte (1.0 M $LiPF_6$ in FEC/EMC/DEC, 3:4:3 by volume), and the TE electrolyte (1.0 M $LiPF_6$ in FEC/EMC/DEC, 3:4:3 by volume, with 2.0 wt.% TMSP). The TE electrolyte shows a slight decrease in ionic conductivity (Table S1) but favorable wettability with the LCO material (Figure S2).

While the TMSP additive has been reported in previous studies, most of the prior work primarily emphasized its optimization effects on the cathode and anode interfaces, without specifically discussing the influences on the electrolyte or detailed evolution mechanism during the electrochemical interfacial processes. In this work, we discovered that, upon introduction, the TMSP molecule first underwent preliminary reactions within the electrolyte. The trimethylsilyl group (-$SiMe_3$) in the TMSP molecule exhibited a strong affinity for fluoride ions (F^-), leading to the release of volatile trimethylsilyl fluoride (TMSF). Thus, when TMSP was introduced into a $LiPF_6$-based electrolyte, the generation of TMSF and the concomitant decomposition of $LiPF_6$ promoted the formation of PF_5 and intermediate species such as bis(trimethylsilyl) phosphate or mono(trimethylsilyl) phosphate [26, 27]. The lone electron pairs on the oxygen atoms of these phosphate esters could then engage in nucleophilic reactions with the strongly Lewis acidic PF_5, yielding fluorophosphate and oligophosphate compounds, which are known as FPD species (Figure 2a) [28, 29].

We verified this reaction pathway using ^{31}P and ^{19}F nuclear magnetic resonance (NMR) spectroscopy. The ^{31}P and ^{19}F NMR spectra of the BE and FE electrolytes showed no signals other than those of PF_6^- (δ_F = −74.0 ppm (d) and δ_P = −144.0 ppm (sept)) (Figure S3). In contrast, the ^{31}P and ^{19}F spectra of the TMSP-containing TE electrolyte revealed distinct new peaks, confirming the formation of phosphorus-containing decomposition products (Figure 2b,c): 1) the ^{19}F peak at δ_F = −158.0 ppm (s) that corresponded to TMSF, 2) the ^{31}P peak at δ_P = −19.2 ppm (t) and ^{19}F peak at δ_F = −84.7 ppm (d) that corresponded to $PO_2F_2^-$, 3) the ^{31}P peak at δ_P = −27.3 ppm (d) and ^{19}F peak at δ_F = −78.6 ppm (d) that corresponded to PO_3F^-, and 4) the ^{31}P peak at $\delta_P < -30$ ppm and ^{19}F peak at $\delta_F > -65$ ppm that represented oligophosphate compounds containing P—O—P chemical bonds [30–32]. Meanwhile, the ^{13}C NMR spectrum showed negligible changes in the peaks corresponding to EC, FEC, EMC, and DEC solvents, respectively (Figure S4) [33]. This indicated that the formation of FPD species primarily originated from reactions involving the anions and the additive components, rather than the decomposition of the solvents.

To further investigate the influence of the FPD components on the electrolyte solvation structure, we conducted ^7Li NMR, Fourier transform infrared (FTIR) spectroscopy, and Raman analyses. A coaxial internal insert that contained a standard NMR solvent (1.0 M LiCl D_2O) was inserted into the NMR tube to enable analysis while preserving the pristine microstructure of the electrolyte, and the same was done in the above-mentioned test. The ^7Li NMR spectra exhibited an upfield shift for both the FE and TE electrolytes, indicating an intensified shielding effect of anions on Li^+, which can be attributed to the weaker ion-dipole interaction between Li^+ and FEC solvent compared to EC (Figure 2d). Furthermore, a distinct line width broadening of the ^7Li NMR signal was observed in the TE electrolyte, suggesting stronger Li^+-anion interactions following the introduction of FPD [34]. This finding of intensified ion pairing was further supported by FTIR results (Figure 2e), which indicated a decrease in solvent-separated ion pairs (SSIPs) and a concurrent increase in contact ion pairs (CIPs) in the TE electrolyte [35, 36]. In line with this, both FTIR and Raman spectra (Figure S5) showed that the TE electrolyte contains a higher relative content of free solvents compared to the FE electrolyte upon the introduction of FPD.

To gain further insight into the microscopic solvation structures, classical molecular dynamics (MD) simulations were employed. For computational simplicity, a small amount of a model compound was introduced, i.e., PO_2F_2-$PO_3(SiMe_3)_2^-$, representing the FPD component with P—O—P species functionalized by F^-/-$SiMe_3$ groups (Figure S6). As shown in Figure 2f, replacing EC with FEC significantly increased the coordination number (CN) of anions within Li^+ solvation sheath, with detailed radial distribution functions (RDFs) and CNs for solvents and anions provided in Figures S7 and S8. Upon the introduction of FPD, the strong ion-dipole interaction between Li^+ and the P═O bonds of the oligophosphate compounds created multiple Li^+-binding sites (Figure S9). These sites were all incorporated into the first solvation shell of Li^+, forming a structure analogous to the

15214095, 0, Downloaded from https://advanced.onlinelibrary.wiley.com/doi/10.1002/adma.73065 by University Town Of Shenzhen, Wiley Online Library on [19/04/2026]. See the Terms and Conditions (https://onlinelibrary.wiley.com/terms-and-conditions) on Wiley Online Library for rules of use; OA articles are governed by the applicable Creative Commons License

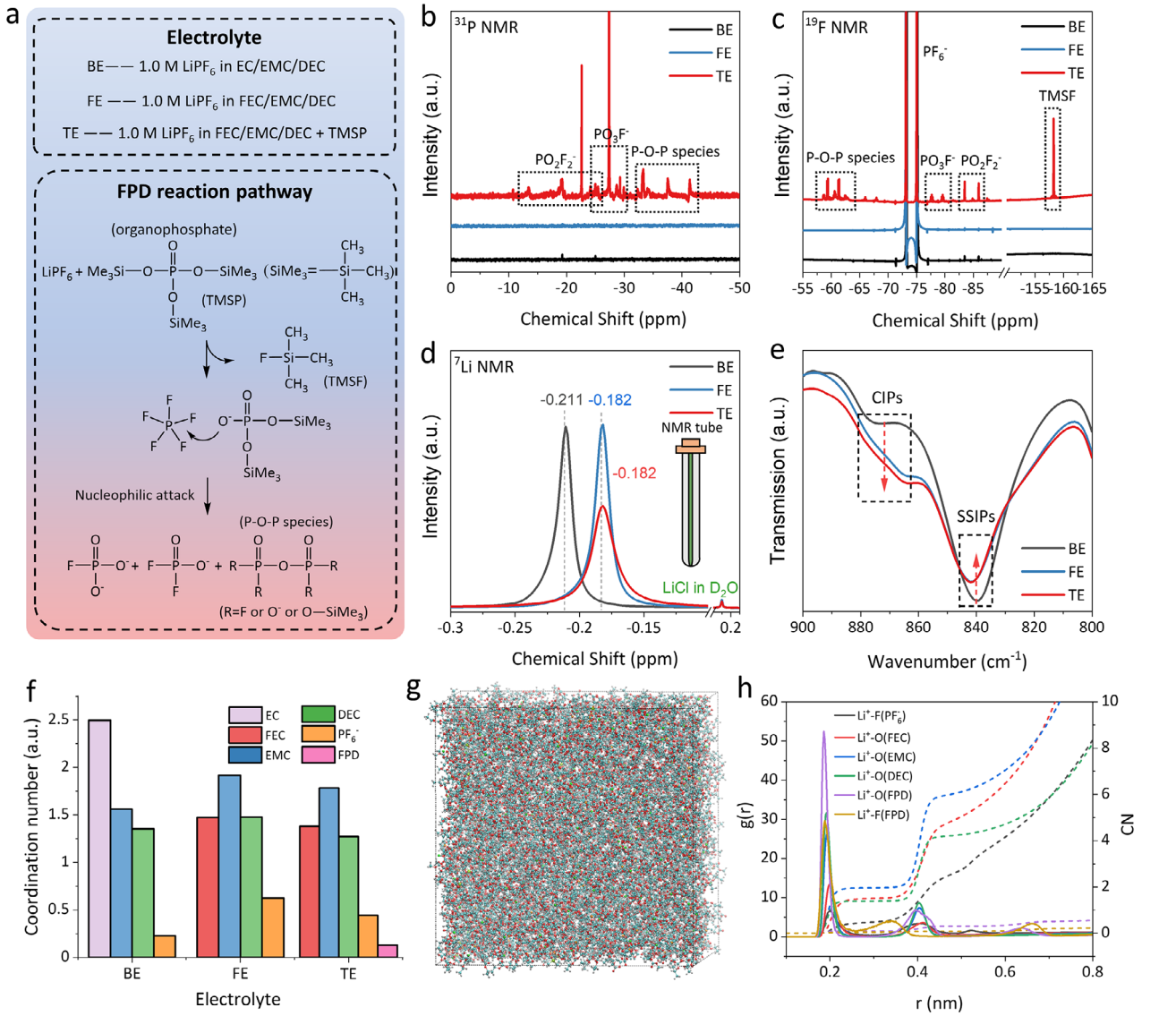

FIGURE 2 | (a) Chemical compositions of the BE, FE, and TE electrolytes and proposed reaction pathway between $LiPF_6$ and TMSP during electrolyte storage. (b) ^{31}P, (c) ^{19}F, and (d) ^{7}Li NMR spectra of three electrolytes. (e) FTIR spectra of three electrolytes. (f) Classical MD simulations of three electrolytes and corresponding CN for solvents and anions within the Li^+ solvation sheath. (g) Snapshots of MD simulation box of the TE electrolyte. (h) The calculated RDFs and CN of TE electrolyte.

aggregates (AGGs) found in high concentrated or localized high-concentration electrolytes. Compared to the FE electrolyte, this mechanism further promoted the participation of anions in the inner solvation shell of TE electrolyte, thereby weakening the interaction between Li^+ and carbonate solvents (Figure 2f–h; Figure S10), establishing the fundamental condition for anion-decomposition-induced formation of a robust CEI.

Furthermore, electrochemical stability was evaluated using linear sweep voltammetry (LSV) and floating tests. The LSV results showed that the TE electrolyte exhibited no significant current increase up to 5 V (Figure S11). In the 4.6 V floating tests conducted on LCO||Li cells at 25°C, cells employing the TE electrolyte exhibited the lowest leakage current among the three electrolyte systems (Figure S12a). When the temperature was raised to 45°C, the kinetics of interfacial side reactions were significantly accelerated, including electrolyte oxidation and cathode structural degradation. Under these conditions (Figure S12b), the TE electrolyte again rapidly suppressed the leakage current to the lowest level, and the magnitude of current increase remained substantially lower than that observed with the BE and FE electrolytes, which confirmed the superior stability of the cathode-electrolyte interface region. Collectively, these preliminary results suggested that the LCO cathode attained enhanced electrochemical and interfacial chemical stability when operated with the TE electrolyte.

3 | Electrochemical Performance of High-Voltage LCO

The modulation of the electrolyte solvation structure significantly influenced the interfacial chemistry and cycling stability of cathode materials. We first examined the evolution of the

15214095, 0, Downloaded from https://advanced.onlinelibrary.wiley.com/doi/10.1002/adma.73065 by University Town Of Shenzhen, Wiley Online Library on [19/04/2026]. See the Terms and Conditions (https://onlinelibrary.wiley.com/terms-and-conditions) on Wiley Online Library for rules of use; OA articles are governed by the applicable Creative Commons License

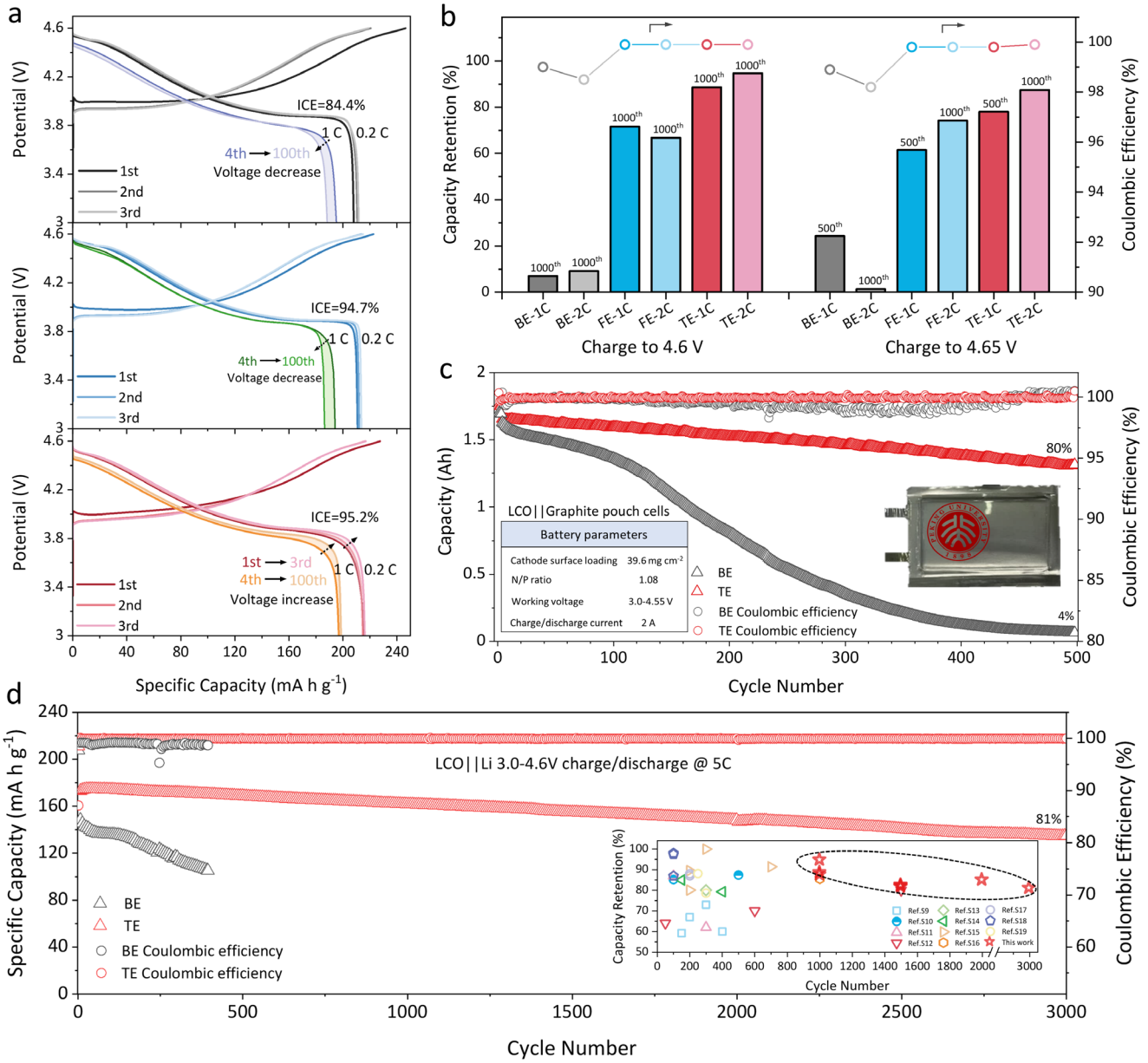

FIGURE 3 | (a) The evolution of the electrochemical profiles in the initial cycles of LCO||Li cells in three electrolytes. (b) Comparison of the long-term cycling stability of LCO||Li cells under upper cutoff voltages of 4.6 and 4.65 V. (c) Cycling performance of high-areal-loading LCO||graphite pouch cells with BE and TE electrolytes. (d) Cycling performance of LCO||Li cells under high-rate operation, with comparison to recently reported literature data.

electrochemical profiles in the initial cycles of LCO||Li cells. Figure 3a shows the voltage curves during the 3.0–4.6 V activation process at 0.2 C (1 C = 200 mA g^{-1}). The initial Coulombic efficiency (ICE) values in the BE, FE, and TE electrolytes were 84.4%, 94.7%, and 95.2%, respectively. This indicated that the complete replacement of EC effectively suppressed interfacial side reactions (as seen with the FE electrolyte), while the introduction of FPD species provided a further improvement, enhancing the interfacial stability of high-voltage LCO. The electrochemical evolution during activation at 1 C also differed markedly among the electrolytes. In the BE electrolyte, the LCO||Li cells exhibited significant capacity loss and voltage polarization within the first 100 cycles, indicating structural degradation of LCO. In contrast, the FE electrolyte, benefiting from FEC's modulation of the Li^+ solvation structure and the reduced Li^+-solvents interaction, improved the rate capability. This resulted in a higher average operating voltage during 1 C cycling and moderately mitigated voltage decay. Notably, the LCO||Li cells in the TE electrolyte showed a distinct activation process at both 0.2 and 1 C rates, characterized by a gradual increase in specific capacity and operating voltage. This suggests a progressive optimization of the LCO interface, leading to enhanced ionic/electronic conductivity and excellent stability [37]. In Figure S13, the comparison of electrochemical profiles and cycling performance under different TMSP addition amounts revealed that as the addition amount increased, the degree of electrochemical activation progressively became more pronounced. Additionally, the 2.0 wt.% TMSP addition was found to balance capacity delivery and cycling

15214095, 0, Downloaded from https://advanced.onlinelibrary.wiley.com/doi/10.1002/adma.73065 by University Town Of Shenzhen, Wiley Online Library on [19/04/2026]. See the Terms and Conditions (https://onlinelibrary.wiley.com/terms-and-conditions) on Wiley Online Library for rules of use; OA articles are governed by the applicable Creative Commons License

performance optimally, representing the most favorable addition amount. The galvanostatic intermittent titration technique (GITT) measurements also confirmed high Li^+ diffusion kinetics in the TE electrolyte during the initial cycles (Figure S14). Further insights from cyclic voltammetry (CV) were shown in Figure S15, which probed the evolution of the surface/interfacial region. The CV curves for LCO in the BE electrolyte showed progressively decreasing peak currents and increasing half-peak widths over 25 cycles. The FE electrolyte effectively reduced the half-peak width and voltage hysteresis, although some degree of structural decay was still evident. In contrast, the TE electrolyte enabled LCO to exhibit continuously decreasing half-peak widths and voltage hysteresis, consistent with the charge and discharge profiles from the initial cycles, underscoring its superior interfacial stability.

The long-term structural stability of LCO was further evaluated in different electrolytes. Figure 3b compares the cycling stability and average Coulombic efficiency of LCO||Li cells under various C-rates and upper cutoff voltages of 4.6 and 4.65 V. A progressive improvement in cycling performance was observed from the BE and FE to the TE electrolyte. The BE electrolyte, suffering from severe interfacial side reactions and structural degradation, delivered the poorest performance. In contrast, the TE electrolyte enabled superior cyclability, achieving a capacity retention of 88.9% after 1000 cycles at 1 C (3.0–4.6 V), 82.5% after 1500 cycles at 1 C (3.0–4.6 V), 94.7% after 1000 cycles at 2 C (3.0–4.6 V), and 85.0% after 2000 cycles at 2 C (3.0–4.6 V). The corresponding voltage profiles are provided in Figures S16 and S17. Charging to a higher cutoff voltage of 4.65 V forces LCO to undergo a greater degree of delithiation, intensifying interfacial side reactions and the degree of phase transition. Despite these harsh conditions, LCO||Li cells with the TE electrolyte maintained a capacity retention of 78.0% after 500 cycles at 1 C (3.0–4.65 V), 87.6% after 1000 cycles at 2 C (3.0–4.65 V), and 81.6% after 2000 cycles at 2 C (3.0–4.65 V), demonstrating exceptional stability. The corresponding voltage profiles are provided in Figures S18 and S19.

Furthermore, the versatility of the TE electrolyte was demonstrated in cells cycled under more extreme conditions. LCO||Li cells achieved an 82.0% capacity retention after 200 cycles at 2 C within a 3.0–4.7 V voltage window (Figure S20a,b). Moreover, when applied to $LiNi_{0.5}Mn_{1.5}O_4$ spinel cathodes cycled within 3.5–5.0 V, the TE electrolyte enabled a high capacity retention of 94.3% over 300 cycles (Figure S20c,d). The practical applicability of the TE electrolyte was further validated in LCO||graphite coin cells and pouch cells. In coin cells (3.0–4.55 V), the TE electrolyte enabled outstanding capacity retentions of 95.3% after 1000 cycles and 86.3% after 1500 cycles, starkly contrasting with the FE (16.4% after 1000 cycles) and BE (0.8% after 1000 cycles) electrolytes (Figure S21). More importantly, high-areal-loading LCO||graphite pouch cells with the TE electrolyte also achieved 80.0% retention after 500 cycles (3.0–4.55 V), confirming its feasibility for practical high-voltage LCO batteries (Figure 3c; Figure S22).

In addition to cycling stability, the TE electrolyte preserved excellent rate capability. As shown in Figure S23, LCO delivered a high specific capacity of 137.2 mAh g^{-1} even at an ultra-high rate of 16 C (3200 mA g^{-1}). Moreover, under a rigorous fast-charging protocol (5 C charge and 5 C discharge), the cell achieved a high capacity retention of 81.0% after 3000 cycles (3.0-4.6 V) (Figure 3d; Figure S24), and 82.0% after 1500 cycles (3.0–4.65 V) (Figure S25). A comparison with recently reported electrolyte engineering strategies for high-voltage LCO highlighted the superior interfacial chemistry and performance advantages conferred by the TE electrolyte system (Figure 3d; Table S2).

4 | Interface Interaction of FPD and LCO

Based on the above results, it was evident that the introduction of FPD species in the TE electrolyte significantly optimized the interfacial chemistry of LCO. To elucidate the underlying improvement mechanism, we employed a combination of in situ attenuated total reflection-Fourier transform infrared (in situ ATR-FTIR) spectroscopy, synchrotron-based soft X-ray absorption spectroscopy (sXAS), in situ differential electrochemical mass spectrometry (DEMS), three-electrode in situ electrochemical impedance spectroscopy (EIS), and first-principles calculations.

The in situ ATR-FTIR results revealed distinct interfacial evolution during the first charging process. The peaks at 840 and 870 cm^{-1} are both associated with PF_6^- and related P-F-containing species, corresponding to uncoordinated and coordinated states, respectively. In the BE electrolyte, the 840 cm^{-1} signal (uncoordinated) gradually accumulated at the LCO interface from lower potentials, while the 870 cm^{-1} signal (coordinated) only showed significant accumulation above 4.5 V (Figure 4a). In contrast, in the TE electrolyte, the 870 cm^{-1} peak intensity increased markedly at lower potentials, suggesting the rapid accumulation of FPD compounds on the LCO surface early in the charging process (Figure 4b). The improved interfacial stability was further corroborated by the analysis of other spectral regions. As shown in Figure S26, for the BE electrolyte, the strong oxidative nature of the highly delithiated LCO surface led to the appearance of distinct signals for —COOH (1490–1570 cm^{-1}) and CO_2 (2300–2400 cm^{-1}), indicating oxidative decomposition of the carbonate solvents. In sharp contrast, the LCO interface in the TE electrolyte exhibited superior stability, with no apparent signals of solvent decomposition, confirming the stable interfacial structure.

Figure 4c presents the O K-edge sXAS spectra in the total electron yield (TEY) mode for pristine LCO, 4.6 V charged state LCO, and 3.0 V discharged state LCO in BE and TE electrolytes. For LCO charged in the BE electrolyte, the spectrum revealed two key features. First, the emergence of peaks at 529 and 527 eV, corresponding to the hybridization of Co^{4+} (e*g)-O 2p and Co^{4+} (t_2g)-O 2p orbitals, confirmed the presence of Co^{4+}. Second, distinct signals were observed at 532 eV and in the 533–538 eV range, which were attributed to electrolyte decomposition products (e.g., Li_2CO_3 and carbonyl species at 532, 533, and 538 eV) and LCO degradation structures (CoO/Co_3O_4 at 531, 535, and 538 eV). Critically, these parasitic products persisted after discharging to 3.0 V, indicating severe and irreversible cathode-electrolyte interface side reactions catalyzed by highly oxidized Co/O ions. In contrast, the surface chemistry of LCO in the TE electrolyte remained highly reversible between the charged (4.6 V) and discharged (3.0 V) states. The spectral features in the TE electrolyte were distinctly different. The peaks in the 532–534 eV range represent the hybridization of Co 3d-O 2p orbitals, reflecting low-valence Co cations. The signals from 534–540 eV correspond to the hybridization of P 3sp-O 2p orbitals (P 3sp

15214095, 0, Downloaded from https://advanced.onlinelibrary.wiley.com/doi/10.1002/adma.73065 by University Town Of Shenzhen, Wiley Online Library on [19/04/2026]. See the Terms and Conditions (https://onlinelibrary.wiley.com/terms-and-conditions) on Wiley Online Library for rules of use; OA articles are governed by the applicable Creative Commons License

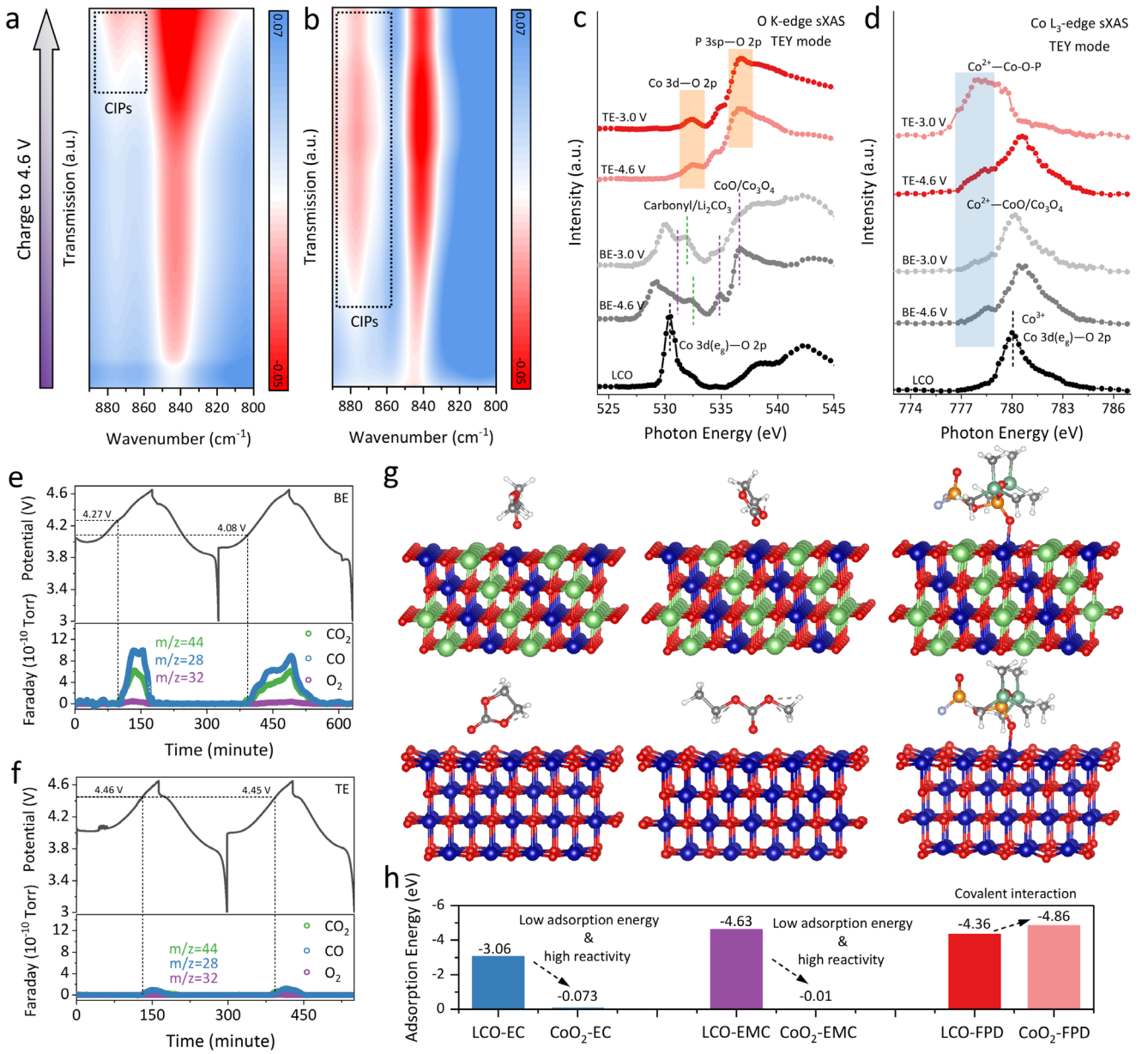

FIGURE 4 | The in situ ATR-FTIR results of the LCO-electrolyte interface region during the first charging process in the (a) BE and (b) TE electrolytes. (c) The O K-edge sXAS spectra (TEY mode) and (d) Co L_3-edge sXAS spectra (TEY mode) for pristine LCO, 4.6 V charged state LCO, and 3.0 V discharged state LCO in BE and TE electrolytes. In situ DEMS tests of LCO||Li cell in the (e) BE and (f) TE electrolytes. (g) Comparison of the adsorption configurations of EC/EMC solvents and FPD species on structural models of the LCO (104) surfaces and its delithiated counterpart (CoO_2), and (h) the calculated adsorption energies.

refers to the sp-hybridized states derived from the P 3s and 3p orbitals) [38, 39]. These signatures confirmed the presence of a surface phosphorus-containing species and suggested a strong covalent interaction with the LCO lattice. These findings were corroborated by the Co L_3-edge sXAS spectra (TEY mode) in Figure 4d. The spectra for LCO in the BE electrolyte showed signatures of both Co^{4+} and cobalt oxides (CoO/Co_3O_4), consistent with surface degradation [40]. Conversely, the spectra for LCO in the TE electrolyte were dominated by signals from low-valence cobalt, indicating that the FPD-induced interfacial reaction effectively stabilized the cobalt in a lower oxidation state, facilitated by the formation of the protective Co—O—P covalent bonding [41].

To minimize interference from the lithium anode interface and better observe the evolution of interfacial side reactions at the LCO cathode, in situ EIS was performed using a three-electrode coin cell configuration (Figure S27). The in situ EIS results and the corresponding distribution of relaxation times (DRT) plots for LCO in the BE and TE electrolytes are shown in Figure S28. The data revealed that LCO in the BE electrolyte exhibited significant interfacial reactions, leading to a continuous and substantial increase in R_{CEI} at voltages ≥4.2 V. In contrast, LCO in the TE electrolyte demonstrated a stable and low R_{CEI}, indicating effective suppression of interfacial side reactions by the FPD components. Furthermore, the strong interaction between the FPD species and the LCO surface resulted in a moderate increase

15214095, 0, Downloaded from https://advanced.onlinelibrary.wiley.com/doi/10.1002/adma.73065 by University Town Of Shenzhen, Wiley Online Library on [19/04/2026]. See the Terms and Conditions (https://onlinelibrary.wiley.com/terms-and-conditions) on Wiley Online Library for rules of use; OA articles are governed by the applicable Creative Commons License

in R_{ct}, a finding consistent with the electrochemical profile evolution observed during the initial cycles.

In situ differential electrochemical mass spectrometry (DEMS) was employed to further validate these observations. The LCO||Li cell with the BE electrolyte exhibited significant signals for CO and CO_2 at voltages above 4.2 V (Figure 4e), indicating severe solvent decomposition. An O_2 signal emerged around 4.5 V, further exacerbating electrolyte oxidation. In sharp contrast, the LCO||Li cell with the TE electrolyte showed markedly suppressed gas evolution (Figure 4f), confirming superior interfacial stability.

First-principles calculations were performed to elucidate the underlying mechanism. Structural models of the LCO (104) surface and its delithiated counterpart (CoO_2) were constructed (Figure 4g). The calculations indicated that EC/EMC solvent molecules initially adsorb on the LCO surface before charging. However, as delithiation proceeds and the cobalt oxidation state increases, the adsorption energy decreases significantly. This weakened interaction was driven by highly oxidative Co^{4+}/O^{n-} ($0<n<2$), ultimately leading to the oxidative decomposition of EC/EMC molecules (Figure 4h). In comparison, the FPD components interacted with both LCO and delithiated LCO surfaces via Co—O—P bonds, promoting their rapid accumulation on the LCO surface during charging and thereby effectively inhibiting side reactions triggered by highly oxidized Co/O sites.

The interfacial chemistry of the cathode material significantly influenced Li^+ (de)intercalation kinetics and the subsequent bulk phase transitions. In situ X-ray diffraction (XRD) analysis provided direct insight (Figure S29). As shown in Figure S29a, LCO cycled in the BE electrolyte exhibited inconsistent high-voltage phase transition behavior during the first two cycles, reflected in varying relative contents and peak positions of the O3, O3/H1-3 hybrid, and H1-3 phases. This indicated markedly non-uniform delithiation across different regions during cycling, which was attributable to heterogeneous and severe side reactions at the LCO surface/interface. In contrast, LCO cycled in the TE electrolyte (Figure S29b) demonstrated highly consistent high-voltage phase transformation patterns between cycles, in alignment with its enhanced interfacial stability. High-resolution transmission electron microscopy (HRTEM) images of LCO at the 4.6 V charged state further supported these findings. Figure S30 showed that LCO cycled in the BE electrolyte exhibited noticeable structural sliding in local regions and an uneven surface spinel phase, whereas LCO cycled in the TE electrolyte maintained good particle integrity with a well-preserved surface layered structure, indicating a uniform delithiation process. These results confirmed that surface-interface chemistry critically governed bulk phase transition behavior, particularly the reversibility of the high-voltage O3–H1-3–O1 phase transition, which became increasingly decisive during long-term cycling.

5 | Characterization of Full-Coverage and Polyphosphates-Based CEI

Based on the aforementioned differences in interfacial reactions, we further characterized the surface and interfacial structure of LCO after 100 cycles. First, the evolution of R_{ct} and R_{CEI} in the BE and TE electrolytes was investigated using in situ EIS with a three-electrode system, combined with the distribution of relaxation times (DRT) analysis. As shown in Figure S31, after cycling in the BE electrolyte, the LCO surface underwent severe structural degradation, evidenced by a shift in the characteristic τ value range from around 10^{-1} s toward 10^{0} s. In contrast, the surface structure of LCO cycled in the TE electrolyte remained well-preserved. Here, the τ values shifted slightly toward higher frequencies, indicating progressively improved interfacial Li^+/electron transport kinetics. Moreover, the CEI formed on LCO in the TE electrolyte exhibited a shift in the characteristic τ value range from approximately 10^{-3} to 10^{-4} s, indicating progressive optimization of its composition and structure. And the interphase remained stable throughout cycling without significant voltage-dependent degradation, ensuring effective protection of the cathode surface. Ex situ EIS measurements at different cycle numbers further supported these findings (Figure S32). The R_{ct} of LCO increased continuously upon cycling in the BE electrolyte, whereas it was effectively suppressed in the FE electrolyte. Notably, the introduction of FPD in the TE electrolyte further reduced R_{ct} to the lowest level, demonstrating the most superior surface and interfacial stability for LCO. These resulted in the lowest R_{ct} values and the most protective CEI, highlighting the critical role of FPD in stabilizing the high-voltage LCO interface.

The surface morphology of the cycled LCO electrodes was examined by scanning electron microscopy (SEM) (Figure S33). In the BE electrolyte, the LCO surface was covered by a sparse and non-uniform CEI layer, accompanied by obvious cracks and slip bands. In contrast, a thick and homogeneous CEI layer fully encapsulated the LCO particles cycled in the TE electrolyte, effectively suppressing detrimental interfacial side reactions. Further cross-sectional characterization using focused ion beam (FIB) milling (Figure 5a,b; Figure S34) revealed significant particle cracking, including both bulk and surface cracks in LCO cycled in the BE electrolyte, along with an uneven CEI distribution. In comparison, LCO cycled in the TE electrolyte exhibited a highly uniform CEI that completely covered the particle surface, providing effective protection. HRTEM with corresponding fast Fourier transform (FFT) patterns was used to examine the near-surface crystal structure. As shown in Figure 5c,e, the surface of LCO cycled in the BE electrolyte contained visible cracks and a spinel-like phase, indicating severe Co/O loss and structural degradation. In contrast, LCO cycled in the TE electrolyte (Figure 5d,f; Figure S35) retained a well-defined layered structure and was covered by a ~100 nm thick CEI layer. Notably, while CEI layers enriched with organic components were often unstable under high-energy electron beams and typically require cryogenic electron microscopy for observation, the CEI in Figure 5d,f remained stable under conventional TEM test conditions and was found to be rich in LiF and Li_3PO_4. For a more systematic compositional analysis while minimizing electron beam damage, cryogenic transmission electron microscopy (cryo-TEM) was additionally employed for interphase characterization [42].

Figure 5g illustrates the sample preparation and characterization procedure of cryo-TEM. Cycled LCO powder was scraped from the electrode in an argon-filled glovebox and deposited onto a TEM copper grid. The copper grid was rapidly vitrified in liquid nitrogen and transferred to a cryo-TEM holder under continuous cooling, maintaining the sample at approximately

15214095, 0, Downloaded from https://advanced.onlinelibrary.wiley.com/doi/10.1002/adma.73065 by University Town Of Shenzhen, Wiley Online Library on [19/04/2026]. See the Terms and Conditions (https://onlinelibrary.wiley.com/terms-and-conditions) on Wiley Online Library for rules of use; OA articles are governed by the applicable Creative Commons License

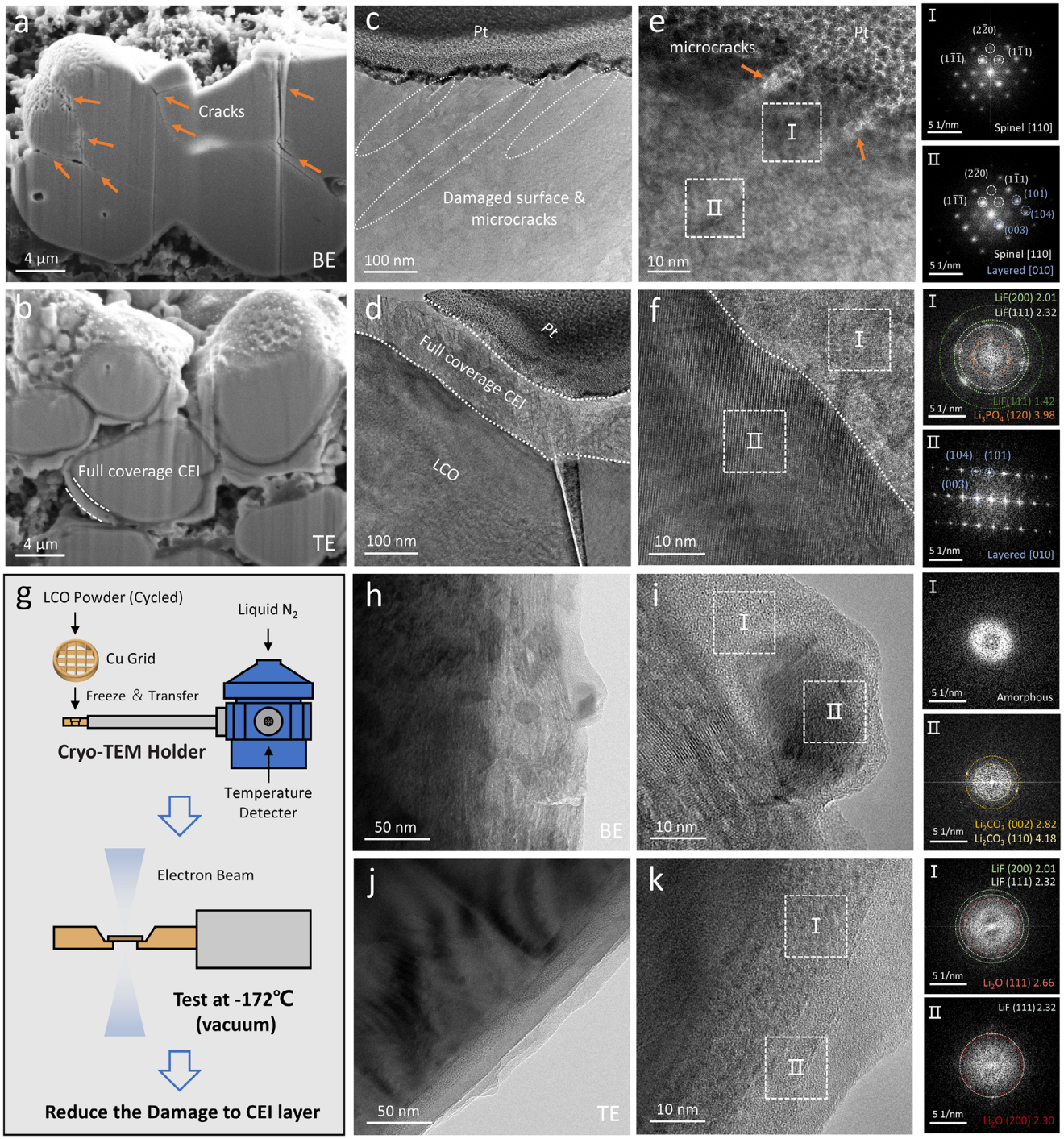

FIGURE 5 | Cross-sectional characterization of LCO cycled in (a) BE and (b) TE electrolytes using FIB milling. The HRTEM images and FFT patterns of LCO cycled in (c,e) BE and (d,f) TE electrolytes. (g) The sample preparation and characterization procedure of cryo-TEM. The cryo-TEM images and FFT patterns of the CEI structure of LCO cycled in the (h,i) BE and (j,k) TE electrolytes.

−172°C during observation to preserve the native state of the CEI [43]. Figure 5h,i, and Figure S36 display the CEI structure of LCO cycled in the BE electrolyte. Visible surface cracks were present, along with a non-uniform coating composed of Li_2CO_3, LiF, amorphous species, and Co_3O_4 spinel, indicating severe interfacial side reactions and lattice oxygen loss. In contrast, LCO cycled in the TE electrolyte exhibited a homogeneous and conformal CEI layer (Figure 5j,k; Figure S37). Compared to conventional TEM observations, the cryo-TEM analysis clearly revealed diffraction rings corresponding to Li_2O within the CEI, a component known to enhance ionic conductivity, while no distinct diffraction rings attributable to Li_3PO_4 were observed. This finding also implied that high-energy electron beams in conventional TEM can induce certain damage to the CEI structure, altering its native composition.

The contrast between the BE and TE electrolytes became even more pronounced when the cutoff voltage was increased from

15214095, 0, Downloaded from https://advanced.onlinelibrary.wiley.com/doi/10.1002/adma.73065 by University Town Of Shenzhen, Wiley Online Library on [19/04/2026]. See the Terms and Conditions (https://onlinelibrary.wiley.com/terms-and-conditions) on Wiley Online Library for rules of use; OA articles are governed by the applicable Creative Commons License

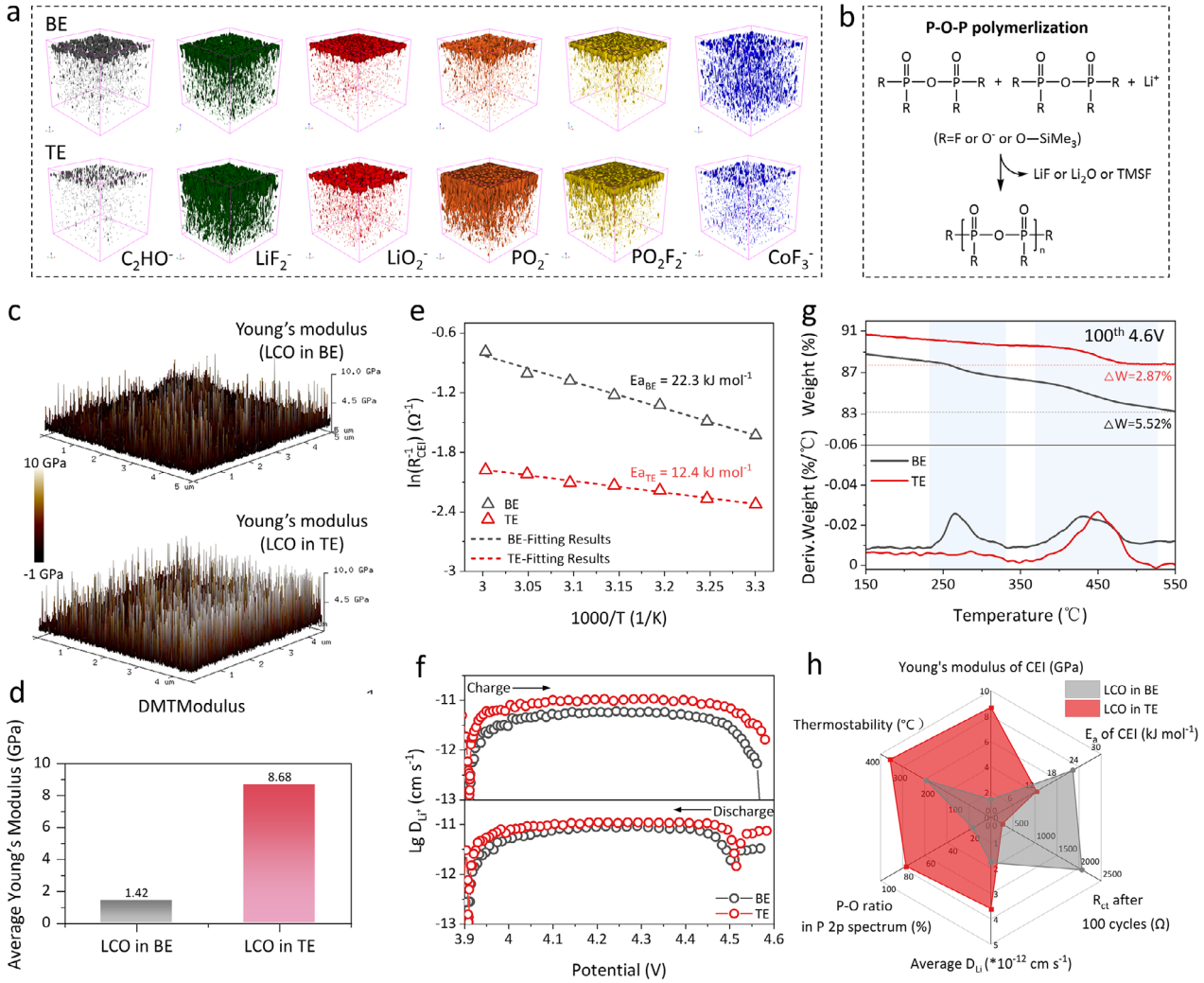

FIGURE 6 | (a) Spatial distribution of CEI components on LCO after cycling in BE and TE electrolytes analyzed by TOF-SIMS. (b) Proposed interfacial reaction scheme of in situ polymerization of surface-anchored FPD compounds on LCO during cycling. (c) Mechanical properties of CEI layers characterized by AFM and (d) comparison of average Young's modulus values in BE and TE electrolytes. (e) Activation energy (*Ea*) for Li^+ transport through the CEI derived from temperature-dependent EIS measurements. (f) Li^+ diffusion coefficients derived from GITT analysis of cycled LCO in BE and TE electrolytes. (g) TG curves of charged (4.6 V) LCO electrodes cycled in BE and TE electrolytes under argon atmosphere. (h) Comprehensive performance comparison of LCO and CEI properties after cycling in BE versus TE electrolytes.

4.6 to 4.65 V. HRTEM (Figure S38) and cryo-TEM (Figure S39) analyses revealed that LCO cycled in the BE electrolyte within 3.0–4.65 V underwent more severe surface structural degradation, interlayer slippage, and particle cracking. In contrast, LCO cycled in the TE electrolyte maintained a stable surface structure and was uniformly covered by a complete CEI layer, which was consistent with the observations at the 4.6 V cutoff voltage.

The spatial distribution of CEI components on LCO after cycling in different electrolytes was analyzed using time-of-flight secondary ion mass spectrometry (TOF-SIMS). As shown in Figure 6a and Figure S40, the CEI formed in the BE electrolyte contained fragments such as C_2HO^-, LiF_2^-, PO_2^-, PO_3^-, POF_2^-, $PO_2F_2^-$, PO_2F^-, etc, which originated from solvent oxidation and the spontaneous decomposition/hydrolysis of $LiPF_6$ at the LCO surface. This was accompanied by severe surface corrosion, as indicated by the presence of CoF_3^- species. In contrast, the FPD-modified interface in the TE electrolyte promoted the accumulation of abundant LiF, Li_2O, P—O, and P—O—F species on the LCO surface. This observation was further supported by the P L-edge sXAS results (Figure S41), which confirmed the enrichment of P—O species on LCO cycled in the TE electrolyte. X-ray photoelectron spectroscopy (XPS) was employed to analyze the CEI composition of LCO after different cycles in LCO||Li cells (Figure S42), as well as in cycled LCO||graphite coin cells and pouch cells (Figure S43) [44]. The results consistently demonstrated that the FPD-induced Co—O—P surface interaction, combined with the oxidation-resistant FEC solvent, led to significantly reduced decomposition products from carbonate solvents (e.g., C—O, C═O, O—C═O, Li_2CO_3, etc.) and a pronounced enrichment of P—O containing species at the interface in the TE electrolyte.

Based on the systematic characterization of CEI morphology and composition, we proposed that the surface-anchored FPD compounds underwent in situ polymerization during cycling (Figure 6b). This polymerization process generated LiF and Li_2O

15214095, 0, Downloaded from https://advanced.onlinelibrary.wiley.com/doi/10.1002/adma.73065 by University Town Of Shenzhen, Wiley Online Library on [19/04/2026]. See the Terms and Conditions (https://onlinelibrary.wiley.com/terms-and-conditions) on Wiley Online Library for rules of use; OA articles are governed by the applicable Creative Commons License

compounds, forming a uniform composite CEI consisting of polyphosphate matrices and inorganic compounds. On the anode side, the TE electrolyte not only suppressed cobalt deposition from the cathode and mitigated the "cross-talk" effects (Figure S44) but also promoted the formation of a stable solid-electrolyte interphase (SEI) on the anode surface. Specifically, XPS analysis (Figure S45) revealed that the TE electrolyte reduced the accumulation of carbonate decomposition products while enriching the SEI with LiF, P—O, and P—O—F species derived from the decomposition of FEC solvent and FPD components. Moreover, in Li||Li symmetric cells, the TE electrolyte enabled uniform Li^+ deposition and stripping on the Li metal anode (Figure S46). This was consistent with morphological observations on the graphite anode in LCO||graphite cells (Figure S47), which showed a smoother and more uniform surface without significant byproduct accumulation [45].

The mechanical, thermodynamic, and kinetic properties of the CEI formed on LCO in the TE electrolyte were further investigated. Atomic force microscopy (AFM) was employed to characterize the mechanical properties of the CEI layers. As shown in Figure 6c,d, the CEI formed in the BE electrolyte exhibited a relatively low Young's modulus, with an average value of only 1.42 GPa. In contrast, the CEI on LCO cycled in the TE electrolyte demonstrated a uniformly distributed Young's modulus, with an average value as high as 8.67 GPa, indicating significantly enhanced mechanical strength. The activation energy (E_a) for Li^+ transport through the CEI was quantitatively determined by temperature-dependent EIS combined with the Arrhenius equation fitting (Figure S48). As illustrated in Figure 6e, the uniform CEI formed in the TE electrolyte exhibited a lower E_a compared to the heterogeneous CEI in the BE electrolyte, corresponding to a reduced energy barrier for Li^+ diffusion. This finding was further supported by GITT and variable-scan-rate CV measurements on cycled LCO electrodes (Figure 6f; Figure S49), which showed that LCO in the TE electrolyte maintained higher Li^+ diffusion coefficients across various voltages after 100 cycles. Thermogravimetric (TG) analysis was performed on charged (4.6 V) LCO electrodes in an argon atmosphere (Figure 6g). The LCO with polyphosphate-based CEI formed in the TE electrolyte demonstrated superior thermal stability: the endothermic peak observed at around 250°C for the BE electrolyte disappeared, and the endothermic peak near 400°C was significantly delayed. These results confirmed the enhanced thermodynamic stability of the CEI in the TE electrolyte. XRD analysis of the discharged LCO electrodes after long-term cycling revealed a pronounced shift and broadening of the (003) peak for the BE electrolyte, indicating severe structural degradation. In contrast, the minimal change in peak position for the TE electrolyte demonstrated exceptional structural stability (Figure S50). In summary, the CEI formed on LCO in the TE electrolyte integrated favorable mechanical strength, high thermal stability, and efficient Li^+ transport kinetics, enabling the low charge-transfer resistance of LCO, and contributing collectively to the outstanding electrochemical performance of high-voltage LCO (Figure 6h).

6 | Conclusion

In conclusion, we demonstrate a targeted construction of a full-coverage and polyphosphates-based CEI for stabilizing high-voltage LCO, induced by FPD electrolyte components. This work reveals that FPD species undergo directed anchoring on the LCO surface during charging, forming a covalent Co—O—P interaction that effectively suppresses the oxidative decomposition of EC and the hydrolysis of $LiPF_6$ triggered by catalytic Co/O sites at high voltages. Simultaneously, the FPD species at the LCO interface undergo in situ polymerization during cycling, resulting in a uniform CEI composed of polyphosphates matrix and inorganic components (LiF/Li_2O), which exhibits favorable mechanical strength, thermal stability, and Li^+ transport kinetics. Coupled with the oxidation-resistant FEC-based solvent system, LCO achieves a capacity retention of 81.0% after 3000 cycles in the voltage range of 3.0–4.6 V and 81.6% after 2000 cycles in the voltage range of 3.0–4.65 V. Importantly, this electrolyte design is also applicable to LCO||graphite pouch cells and can be even extended to 4.7 V high-voltage LCO and 5 V $LiNi_{0.5}Mn_{1.5}O_4$ cathode systems. This work provides valuable insights and a strategic guideline for interfacial design in advanced high-voltage cathode materials.

Acknowledgment

This work was financially supported by the China Postdoctoral Science Foundation (No. 2025M780009), National Center for International Research of Power Batteries and Materials (No. 2015B01015), Guangdong Key Laboratory of Design and Calculation of New Energy Materials (No. 2017B030301013), Shenzhen Key Laboratory of New Energy Resources Genome Preparation and Testing (No. SYSPG20241211173440007). We also thank the staff members of the XMCD beamline and at the National Synchrotron Radiation Laboratory in Hefei, for providing the technical support and assistance in data collection and analysis.

Funding

China Postdoctoral Science Foundation (2025M780009), National Center for International Research of Power Batteries and Materials (2015B01015), Guangdong Key Laboratory of Design and calculation of New Energy Materials (2017B030301013), Shenzhen Key Laboratory of New Energy Resources Genome Preparation and Testing (SYSPG20241211173440007).

Conflicts of Interest

The authors declare no conflict of interest.

Data Availability Statement

The data that support the findings of this study are available from the corresponding author upon reasonable request.

References

1. K. Mizushima, P. C. Jones, P. J. Wiseman, and J. B. Goodenough, "Li_xCoO_2(O<x≤1): A New Cathode Material for Batteries of High Energy Density," *Materials Research Bulletin* 15 (1980): 783–789.

2. Y. Huang, "The Discovery of Cathode Materials for Lithium-Ion Batteries from the View of Interdisciplinarity," *Interdisciplinary Materials* 1 (2022): 323–329.

3. W. Zhao, M. Li, Z. Li, et al., "Stabilizing Surface Lattice O^{n-} (0<n<2) for Long-Term Durability of $LiCoO_2$," *Angewandte Chemie International Edition* 64 (2025): 202503100.

4. H. Ren, G. Zheng, Y. Li, et al., "Stabilizing $LiCoO_2$ at 4.6 V by Regulating Anti-oxidative Solvents," *Energy & Environmental Science* 17 (2024): 7944–7957.

15214095, 0, Downloaded from https://advanced.onlinelibrary.wiley.com/doi/10.1002/adma.73065 by University Town Of Shenzhen, Wiley Online Library on [19/04/2026]. See the Terms and Conditions (https://onlinelibrary.wiley.com/terms-and-conditions) on Wiley Online Library for rules of use; OA articles are governed by the applicable Creative Commons License

5. Q. Wang, Z. Yao, J. Wang, et al., "Chemical Short-range Disorder in Lithium Oxide Cathodes," *Nature* 629 (2024): 341–347.

6. T. Zhou, L. Chen, H. Zhang, et al., "Tuning Interfacial Solvent Orientation for High-voltage Lithium-ion Batteries," *Chemistry* 12 (2025): 102819.

7. X. Wang, D. Ren, H. Liang, et al., "Ni Crossover Catalysis: Truth of Hydrogen Evolution in Ni-rich Cathode-based Lithium-ion Batteries," *Energy & Environmental Science* 16 (2023): 1200–1209.

8. Y. Zhang, Y. Katayama, R. Tatara, et al., "Revealing Electrolyte Oxidation via Carbonate Dehydrogenation on Ni-based Oxides in Li-ion Batteries by in Situ Fourier Transform Infrared Spectroscopy," *Energy & Environmental Science* 13 (2020): 183–199.

9. B. L. D. Rinkel, D. S. Hall, I. Temprano, and C. P. Grey, "Electrolyte Oxidation Pathways in Lithium-Ion Batteries," *Journal of the American Chemical Society* 142 (2020): 15058–15074.

10. W. Ding, H. Ren, Z. Li, et al., "Tuning Surface Rock-Salt Layer as Effective O Capture for Enhanced Structure Durability of $LiCoO_2$ at 4.65 V," *Advanced Energy Materials* 14 (2024): 2303926.

11. H. Y. Asl and A. Manthiram, "Reining in Dissolved Transition-metal Ions," *Science* 369 (2020): 140–141.

12. H. Ren, W. Zhao, H. Yi, et al., "One-Step Sintering Synthesis Achieving Multiple Structure Modulations for High-Voltage $LiCoO_2$," *Advanced Functional Materials* 33 (2023): 2302622.

13. X. Wang, H. Ren, Y. Du, et al., "Tuning Surface Chemistry to Reduce the Step-Like Degradation of $LiCoO_2$ at 4.6 V," *Nano Energy* 125 (2024): 109537.

14. K. Xu, "Interfaces and Interphases in Batteries," *Journal of Power Sources* 559 (2023): 232652.

15. A. Zhang, E. Yang, Z. Bi, et al., "Unlocking 4.7 V $LiCoO_2$ with a Counterintuitive Low-Concentration Fluoroborate Dual-Salt Electrolyte by Anion-Derived Interfacial Chemistry," *ACS Energy Letters* 10 (2025): 1245–1254.

16. C. Weng, M. Qiu, B. Wang, et al., "Organic Cathode Electrolyte Interphase Achieving 4.8 V $LiCoO_2$," *Angewandte Chemie* 137 (2025): 202419539.

17. Q. Wu, M. Fang, S. Jiao, et al., "Phase Regulation Enabling Dense Polymer-based Composite Electrolytes for Solid-state Lithium Metal Batteries," *Nature Communications* 14 (2023): 6296, https://doi.org/10.1038/s41467-023-41808-3.

18. W. Sun, Q. Yu, S. Wang, et al., "Dual-salt-additive Reinforced Commercial Carbonate-based Electrolytes for 4.7 V High-voltage Practical Li-ion and Li-metal Batteries," *Energy Storage Materials* 82 (2025): 104627.

19. Q. Xiong, R. Wang, D. Li, et al., "Covalent and Polyfluorinated Lithium Salt for Stable $LiCoO_2$ Batteries at High Temperature and High Voltage," *Nature Communications* 16 (2025): 10325.

20. H. Ren, X. Wang, W. Ding, et al., "Electrochemical Self-Assembly of Boron-Based Cathode-Electrolyte Interphase to Stabilize 4.65 V $LiCoO_2$," *Advanced Functional Materials* 35 (2025): 2504165.

21. H. Ren, J. Hu, H. Ji, et al., "Densification of Cathode/Electrolyte Interphase to Enhance Reversibility of $LiCoO_2$ at 4.65 V," *Advanced Materials* 36 (2024): 2408875.

22. V. A. Maske and A. P. More, "Conformal Coatings for Lithium-ion Batteries: A Comprehensive Review," *Progress in Organic Coatings* 188 (2024): 108252.

23. D. Lu, R. Li, L. Lv, et al., "Tailoring Cathode Interphase Chemistry for High-Voltage Li-Ion Batteries," *Angewandte Chemie International Edition* 65 (2025): 18546.

24. G. Zheng, H. Ren, J. Qiu, et al., "Additive-Regulated Interface Chemistry Enables Depolarization for Ultra-High Capacity $LiCoO_2$," *Advanced Materials* 37 (2025): 04106.

25. T. Zhou, J. Wang, L. Lv, et al., "Anion–π Interaction and Solvent Dehydrogenation Control Enable High-voltage Lithium-ion Batteries," *Energy & Environmental Science* 17 (2024): 9185–9194.

26. A. Jamal, G. D. Salian, A. Mathew, et al., "Tris(trimethylsilyl) Phosphite and Lithium Difluoro(oxalato)Borate as Electrolyte Additives for $LiNi_{0.5}Mn_{1.5}O_4$ -Graphite Lithium-Ion Batteries," *ChemElectroChem* 10 (2023): 202300139.

27. N. Gogoi, E. Bowall, R. Lundström, et al., "Silyl-Functionalized Electrolyte Additives and Their Reactivity toward Lewis Bases in Li-Ion Cells," *Chemistry of Materials* 34 (2022): 3831–3838.

28. L. A. Wessjohann and M. A. Dessoy, "An Efficient Method for the Preparation of Silyl Esters of Diphosphoric, Phosphoric, and Phosphorous Acid," *Polyhedron* 70 (2014): 133–137.

29. X. Qi, L. Tao, H. Hahn, et al., "Lifetime Limit of Tris(trimethylsilyl) Phosphite as Electrolyte Additive for High Voltage Lithium Ion Batteries," *Rsc Advances* 6 (2016): 38342–38349.

30. X. Yang, M. Lin, G. Zheng, et al., "Enabling Stable High-Voltage $LiCoO_2$ Operation by Using Synergetic Interfacial Modification Strategy," *Advanced Functional Materials* 30 (2020): 2004664.

31. P. J. Buitrago Botero, A. W. Ells, A. Svirinovsky-Arbeli, M. Juelsholt, and L. E. Marbella, "Counterion Lewis Acidity Determines the Rate of Hexafluorophosphate Hydrolysis in Nonaqueous Battery Electrolytes," *Journal of the American Chemical Society* 147 (2025): 9159–9174.

32. D. Mu, Y. Liu, R. Li, Q. Ma, and C. Dai, "Transcritical CO_2 Extraction of Electrolytes for Lithium-ion Batteries: Optimization of the Recycling Process and Quality–quantity Variation," *New Journal of Chemistry* 41 (2017): 7177–7185.

33. L. Yang, A. Xiao, and B. L. Lucht, "Investigation of Solvation in Lithium Ion Battery Electrolytes by NMR Spectroscopy," *Journal of Molecular Liquids* 154 (2010): 131–133.

34. H. Chen, K. Chen, J. Yang, et al., "Designing Advanced Electrolytes for High-Safety and Long-Lifetime Sodium-Ion Batteries via Anion–Cation Interaction Modulation," *Journal of the American Chemical Society* 146 (2024): 15751–15760.

35. J. Zheng, J. A. Lochala, A. Kwok, Z. D. Deng, and J. Xiao, "Research Progress towards Understanding the Unique Interfaces between Concentrated Electrolytes and Electrodes for Energy Storage Applications," *Advanced Science* 4 (2017): 1700032.

36. D. M. Seo, O. Borodin, S. Han, Q. Ly, P. D. Boyle, and W. A. Henderson, "Electrolyte Solvation and Ionic Association," *Journal of the Electrochemical Society* 159 (2012): A553–A565.

37. M. Shang, H. Ren, W. Zhao, et al., "Alleviating Structure Collapse of Polycrystalline $LiNi_XCo_yMn_{1-x-Y}O_2$ via Surface Co Enrichment," *ACS NANO* 18 (2024): 16982–16993.

38. T. Jenkins, J. A. Alarco, B. Cowie, and I. D. R. Mackinnon, "Regulation of Surface Oxygen Activity in Li-rich Layered Cathodes Using Band Alignment of Vanadium Phosphate Surface Coatings," *Journal of Materials Chemistry A* 10 (2022): 24487–24509.

39. T. Jenkins, J. A. Alarco, B. Cowie, and I. D. R. Mackinnon, "Direct Spectroscopic Observation of the Reversible Redox Mechanism in A3V2(PO4)3(A = Li,Na) Cathode Materials for Li-ion Batteries," *Journal of Power Sources* 571 (2023): 233078.

40. C. Yogi, D. Takamatsu, K. Yamanaka, et al., "Soft X-Ray Absorption Spectroscopic Studies with Different Probing Depths: Effect of an Electrolyte Additive on Electrode Surfaces," *Journal of Power Sources* 248 (2014): 994–999.

41. S. Neudeck, F. Walther, T. Bergfeldt, et al., "Molecular Surface Modification of NCM622 Cathode Material Using Organophosphates for Improved Li-Ion Battery Full-Cells," *Acs Applied Materials & Interfaces* 10 (2018): 20487–20498.

42. Y. Li, Y. Li, A. Pei, et al., "Atomic Structure of Sensitive Battery Materials and Interfaces Revealed by Cryo–electron Microscopy," *Science* 358 (2017): 506–510.

15214095, 0, Downloaded from https://advanced.onlinelibrary.wiley.com/doi/10.1002/adma.73065 by University Town Of Shenzhen, Wiley Online Library on [19/04/2026]. See the Terms and Conditions (https://onlinelibrary.wiley.com/terms-and-conditions) on Wiley Online Library for rules of use; OA articles are governed by the applicable Creative Commons License

43. Z. Zhang, J. Yang, W. Huang, et al., "Cathode-Electrolyte Interphase in Lithium Batteries Revealed by Cryogenic Electron Microscopy," *Matter* 4 (2021): 302–312.

44. J. Zhang, Q. Li, Y. Wang, J. Zheng, X. Yu, and H. Li, "Dynamic Evolution of Cathode Electrolyte Interphase (CEI) on High Voltage $LiCoO_2$ Cathode and Its Interaction with Li Anode," *Energy Storage Materials* 14 (2018): 1–7.

45. Y. Liang, F. A. C. Apfelbeck, K. Sun, et al., "Unveiling the Li/Electrolyte Interface Behavior for Dendrite-Free All-Solid-State Lithium Metal Batteries by Operando Nano-Focus WAXS," *Advanced Science* 12 (2025): 2414714.

Supporting Information

Additional supporting information can be found online in the Supporting Information section.

Supporting File: adma73065-sup-0001-SuppMat.docx.

15214095, 0, Downloaded from https://advanced.onlinelibrary.wiley.com/doi/10.1002/adma.73065 by University Town Of Shenzhen, Wiley Online Library on [19/04/2026]. See the Terms and Conditions (https://onlinelibrary.wiley.com/terms-and-conditions) on Wiley Online Library for rules of use; OA articles are governed by the applicable Creative Commons License